Fractal character of the neural spike train in the visual system of the cat

Malvin C. Teich

*Departments of Electrical and Computer Engineering, Biomedical Engineering, and Cognitive and Neural Systems,
Boston University, Boston, Massachusetts 02215*

Conor Heneghan

*Department of Electrical and Computer Engineering, Boston University, Boston, Massachusetts 02215,
and New York Eye and Ear Infirmary, New York, New York 10003*

Steven B. Lowen

Department of Electrical and Computer Engineering, Boston University, Boston, Massachusetts 02215

Tsuyoshi Ozaki and Ehud Kaplan

*The Mount Sinai School of Medicine, New York, New York 10029, and The Rockefeller University, New York,
New York 10021*

We used a variety of statistical measures to identify the point process that describes the maintained discharge of retinal ganglion cells (RGC's) and neurons in the lateral geniculate nucleus (LGN) of the cat. These measures are based on both interevent intervals and event counts and include the interevent-interval histogram, rescaled range analysis, the event-number histogram, the Fano factor, the Allan factor, and the periodogram. In addition, we applied these measures to surrogate versions of the data, generated by random shuffling of the order of interevent intervals. The counting statistics reveal $1/f$-type fluctuations in the data (long-duration power-law correlation), which are not present in the shuffled data. Estimates of the fractal exponents measured for RGC- and their target LGN-spike trains are similar in value, indicating that the fractal behavior either is transmitted from one cell to the other or has a common origin. The gamma-r renewal process model, often used in the analysis of visual-neuron interevent intervals, describes certain short-term features of the RGC and LGN data reasonably well but fails to account for the long-duration correlation. We present a new model for visual-system nerve-spike firings: a gamma-r renewal process whose mean is modulated by fractal binomial noise. This fractal, doubly stochastic point process characterizes the statistical behavior of both RGC and LGN data sets remarkably well. © 1997 Optical Society of America [S0740-3232(97)00202-0]

1. INTRODUCTION

The sequence of action potentials recorded from cat retinal ganglion cells[1–16] (RGC's) and lateral-geniculate-nucleus (LGN) cells[17–21] remains irregular even when the retina is thoroughly adapted to a steady stimulus of fixed luminance. The statistical properties of these spike trains has generally been investigated from the point of view of the interevent-interval histogram (IIH), which provides a measure of the relative frequency of intervals of different durations. The mathematical model most widely used to describe the IIH is the gamma renewal process (GRP), though point processes incorporating refractoriness[1,4,8,10,11,14] have also been investigated.

However, there are properties of a sequence of action potentials, such as long-duration correlation or memory, that cannot generally be inferred from measures that reset at short times, like the IIH.[22] The ability to distinguish features such as these demands the use of measures such as the event-number histogram (ENH) or the periodogram (PG), which can extend over time (or fre-

quency) scales corresponding to many events. In this paper we examine the variability and correlation properties of the maintained discharge from RGC and LGN neurons over a broad range of time scales. The analysis of these discharges reveals that the spikes behave as fractal sequences.

Fractals are objects that possess a form of self-similarity: Parts of the whole can be made to fit to the whole by shifting and stretching. In the context of a one-dimensional stochastic point process, a fractal data set exhibits clustering, with smaller clusters of events forming part of larger clusters of clusters and so forth, over a range of cluster sizes. The hallmark of fractal behavior is power-law dependence in one or more statistical measures, over a substantial range of the time or frequency scale at which the measurement is conducted.[23] Fractal signals are also said to be self-similar or self-affine.

Perhaps the simplest example of a measure that reveals fractal behavior in the spike train is provided by the estimated rate of neural firing, which is displayed in

Fig. 1(a) for the maintained discharge of a cat LGN cell. The rate estimate is formed by dividing the number of spikes in successive counting windows of duration T by the counting time T. The rate estimate of the randomly shuffled version of the data is presented in Fig. 1(b).

From a comparison of Figs. 1(a) and 1(b) it is apparent that the magnitude of the rate-estimate fluctuations decreases more slowly with increasing counting time for the original data than for the shuffled version. Fractal processes exhibit slow power-law convergence: The standard deviation of the rate decreases more slowly than $1/\sqrt{T}$ as the averaging time increases.[24] Nonfractal signals, such as the shuffled LGN spike train, on the other hand, exhibit fluctuations that decrease precisely as $1/\sqrt{T}$. The shuffling process removes the fractal character of the spike train by destroying the long-term correlation among the interevent intervals. Since both the data and its shuffled surrogate possess the same IIH, it is quite clear that the IIH does not reveal the long-duration correlation present in the data at hand.

Fractal behavior is ubiquitous in sensory systems. Its presence has been observed in cat striate-cortex neural spike trains,[25] and in the spike train of a locust visual interneuron, the descending contralateral movement detector.[26] It is present in the auditory system of a number of species; primary auditory (VIII-nerve) nerve fibers in the cat,[27-31] the chinchilla,[32] and the chicken[33] all exhibit fractal behavior. It is present at many biological levels, from the microscopic to the macroscopic[34,35]; examples include ion-channel behavior,[27,36-38] neurotransmitter exocytosis at the synapse,[39] spike trains in rabbit somatosensory-cortex neurons,[40] spike trains in mesencephalic reticular-formation neurons,[41] and even the sequence of human heartbeats.[42,43] In almost all cases the upper limit of the observed time over which fractal correlations exist is imposed by the duration of the recording.

The GRP cannot describe the fractal behavior present in RGC and LGN spike trains. Indeed, no nonfractal renewal process can do so, since memory is required. We therefore construct a fractal, doubly stochastic point process that incorporates multiscale fluctuations into the gamma-r renewal process. We show that this process provides a good description for the characteristics of the RGC and LGN maintained discharges.

In Section 2 we briefly outline the techniques used to acquire RGC and LGN nerve-spike trains, and in Section 3 we present the theoretical background for the statistical measures that we utilize. The results are reported in Section 4, and the gamma-based fractal stochastic point-process (FSPP) model is framed in Section 5. The discussion is provided in Section 6, where the relative merits of other FSPP models are set forth.
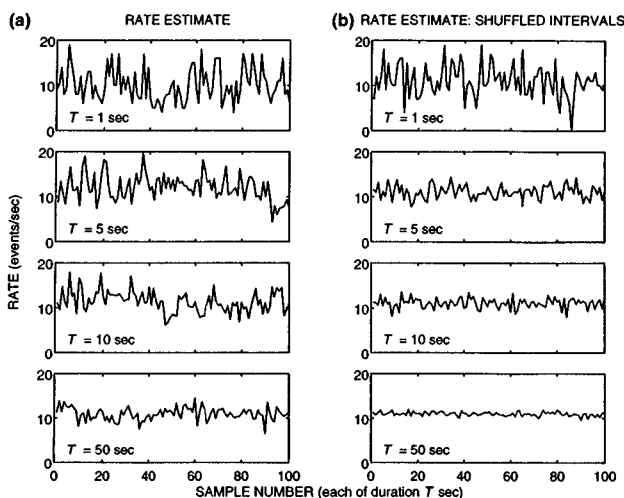

Fig. 1.   Rate estimates formed by dividing the number of events in successive counting windows by the counting time T.   (a) Rate estimate for a cat lateral-geniculate-nucleus (LGN) cell (file name MD2-LGN) generated with the use of four different counting times ($T = 1, 5, 10,$ and 50 s). The fluctuations in the rate estimate converge relatively slowly as the counting time is increased. This is characteristic of fractal processes. The convergence properties are quantified by event-number measures such as the rate standard deviation (RSD), the Fano factor (FF), the Allan factor (AF), and the periodogram (PG).   (b) Rate estimates from the same recording as that in (a) after the intervals are randomly reordered (shuffled). This maintains the same relative frequency of interval sizes but destroys long-term correlations (and therefore the fractal behavior) arising from other sources, such as rate fluctuations. For such nonfractal signals the rate estimate converges more quickly as the counting time T is increased. The stimulus was a uniformly illuminated screen (with no temporal or spatial modulation) of luminance 33 cd/m^2. The data presented here are typical of the 26 data sets examined.

2. MATERIALS AND METHODS

The experimental methods are similar to those used by Kaplan and Shapley.[44] Experiments were carried out on adult cats. Anesthesia was induced by intramuscular (IM) injection of xylazine (Rompun 2 mg/kg), followed 10 min later by IM injection of ketamine HCl (Ketaset 10 mg/kg). Anesthesia was maintained during surgery with intravenous (IV) injections of thiamylal (Surital 2.5%) or thiopental (Pentothal 2.5%). During recording, anesthesia was maintained with Pentothal [2.5%, 2–6 (mg/kg)/h]. The local anesthetic Novocain was administered, as required, during the surgical procedures. Penicillin (750,000 units IM) was also administered to prevent infection, as was dexamethasone (Decadron, 6 mg IV) to forestall cerebral edema. Muscular paralysis was induced and maintained with gallium triethiodide [Flaxedil, 5–15 (mg/kg)/h] or vecuronium bromide [Norcuron, 0.25 (mg/kg)/h]. Infusions of Ringer's saline with 5% dextrose at 3–4 (ml/kg)/h were also administered.

The two femoral veins and a femoral artery were cannulated for IV drug infusions. Heart rate and blood pressure, along with expired CO_2, were continuously monitored and maintained in physiological ranges. For male cats the bladder was also cannulated to monitor fluid outflow. Core body temperature was maintained at 37.5 °C throughout the experiment by wrapping the animal's torso in a dc heating pad controlled by feedback from a subscapular temperature probe. The cat's head was fixed in a stereotaxic apparatus. The trachea was cannulated to allow for artificial respiration. To minimize respiratory artifacts, the animal's body was suspended from a vertebral clamp and a pneumothorax was performed when needed.

Eyedrops of 10% phenylephrine hydrochloride (Neo-synephrine) and 1% atropine were applied to dilate the pupils and retract the nictitating membranes. Gas-permeable hard contact lenses protected the corneas from drying. Artificial pupils of 3-mm diameter were placed in front of the contact lenses to maintain fixed retinal illu-mination. The optical quality of the animal's eyes was regularly examined by ophthalmoscopy. The optic disks were mapped onto a tangent screen, by backprojection, for use as a positional reference. The animal viewed a uni-formly illuminated CRT screen (Tektronix 608, 270 frames/s, or CONRAC, 135 frames/s) with a fixed lumi-nance level.

A craniotomy was performed over the LGN (center lo-cated 6.5 mm anterior to the earbars and 9 mm lateral to the midline of the skull), and the dura mater was re-sected. A tungsten-in-glass microelectrode (5–10-μm tip length)[45] was lowered until spikes from a single LGN neuron were isolated. The microelectrode simulta-neously recorded RGC activity, in the form of S poten-tials, and LGN spikes, with a timing accuracy of 0.1 ms. The output was amplified and monitored using conven-tional techniques. A cell was classified as Y-type if it ex-hibited strong frequency doubling in response to contrast-reversing high-spatial-frequency gratings and X-type otherwise.[46,47]

The experimental protocol was approved by the Animal Care and Use Committee of Rockefeller University and was in accord with the National Institutes of Health guidelines for the use of higher mammals in neuroscience experiments.

3. ANALYSIS TECHNIQUES

A. Point Processes

The statistical behavior of a nerve-spike train can be studied by replacing the complex waveform of an indi-vidual action potential recorded electrically by a single number that records the time of the peak (or other desig-nator) of the action potential. In mathematical terms the nerve-spike train is then viewed as an unmarked point process. This simplification greatly reduces the compu-tational complexity of the problem and permits us to use the substantial methodology previously developed for sto-chastic point processes.

The occurrence of a nerve spike at time t_i is therefore simply represented by an impulse $\delta(t - t_i)$ at that time, so that the sequence of action potentials is represented by

$$s(t) = \sum_i \delta(t - t_i). \tag{1}$$

As illustrated in Fig. 2(a), a realization of a point process is specified by the set of occurrence times $\{t_i\}$ of the events. A single realization of the data is generally all that is available to the observer, so that the identification of the point process, and the elucidation of the mecha-nisms that underlie it, must be gleaned from this one re-alization.

One way in which the information in an experimental sequence of events can be made more digestible is to re-duce the data into a statistic that emphasizes a particular

aspect of the data at the expense of other features. These statistics fall into two broad classes,[22,48] which have their origins, respectively, in the sequence of interevent inter-vals $\{\tau_i\}$ [to be distinguished from the occurrence times
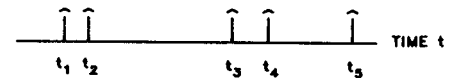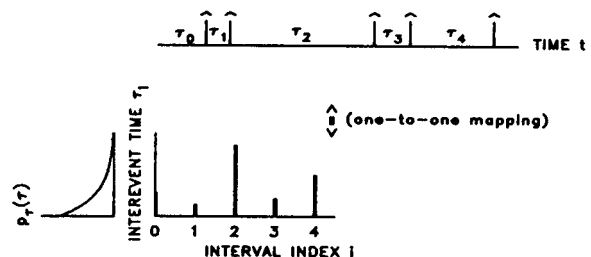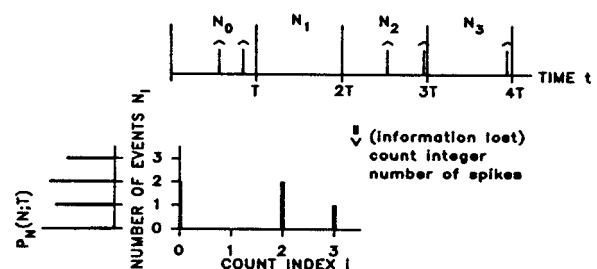

Fig. 2. (a) The sequence of action-potential waveforms is re-duced to a set of event occurrence times $\{t_i\}$ that form a point process. (b) A sequence of interevent intervals $\{\tau_i\}$ is formed from the time between successive events, resulting in a discrete-time, positive, real-valued stochastic process. All information contained in the original point process is preserved in this repre-sentation, but the discrete-time axis of the sequence of interevent intervals is randomly distorted relative to the real-time axis of the point process. (c) The sequence of counts $\{N_i\}$, a discrete-time, nonnegative, integer-valued stochastic process, is formed from the point process by recording the numbers of events in suc-cessive counting windows of duration T. Information is lost in mapping the point process to the sequence $\{N_i\}$, but the amount lost can be made arbitrarily small by reducing T. An advan-tage of this representation is that no distortion of the time axis occurs.

$\{t_i\}$], represented in Fig. 2(b), and in the sequence of counts $\{N_i\}$, represented in Fig. 2(c). Measures based on interval and counting statistics are discussed in Subsections 2.B and 2.C, in turn.

We first consider the homogeneous Poisson point process (HPP), which is the simplest of all stochastic point processes.[49] It is described by a single parameter, the rate λ. The HPP is memoryless: the occurrence of an event at any time t_0 is independent of the presence (or the absence) of events at other times $t \neq t_0$. Because of this property, both the intervals $\{\tau_i\}$ and the counts $\{N_i\}$ form sequences of independent, identically distributed (iid) random variables. The HPP interval process is therefore completely characterized by the interevent-interval distribution (which is exponential) or the event-number distribution (which is Poisson). The HPP serves as a benchmark against which other point processes are measured and therefore plays the role that the white Gaussian process plays in the realm of continuous-time stochastic processes.[50]

A related point process is the nonparalyzable fixed-dead-time-modified Poisson point process (DTMP),[51] a close cousin of the HPP that differs only by the imposition of a dead-time (refractory) interval after the occurrence of each event, during which other events are prohibited from occurring. Another cousin is the gamma-r renewal process[48] (GRP) which, for integer r, is generated from a HPP by permitting every rth event to survive while deleting all other events. Both the DTMP and the GRP require two parameters for their description. Both of these, as well as the HPP, belong to the class of renewal point processes, which will be defined in Section 3.B.

However, nonrenewal point processes are required to describe spike trains in the visual system. Of particular interest are fractal stochastic point processes (FSPP's), in which one or more statistics exhibit power-law behavior.[23] One feature of such processes is the relatively slow (power-law) convergence of the rate estimate, as illustrated in Fig. 1(a).

B. Interevent-Interval Measures of a Point Process

We employ two statistical measures to characterize the discrete-time stochastic process $\{\tau_i\}$, which is a sequence of positive real-valued random variables, as illustrated in Fig. 2(b). These are the IIH and rescaled range analysis (R/S).

1. Interevent-Interval Histogram

The IIH (often referred to as the interspike-interval histogram, or ISI, in the physiology literature) displays the relative frequency of occurrence $p_\tau(\tau)$ of an interval of size τ; it is an estimate of the probability-density function of interevent-interval magnitude [see Fig. 2(b)]. It is, perhaps, the most commonly used of all statistical measures of point processes in the life sciences. The IIH provides information about the underlying process over time scales that are of the order of the interevent intervals. Its construction involves the loss of interval ordering and therefore dependencies among intervals; a reordering of the sequence $\{\tau_i\}$ does not alter the IIH, since the order plays no role in the relative frequency of occurrence.

Some point processes exhibit no dependencies among their interevent intervals at the outset, in which case the sequence of interevent intervals forms a sequence of iid random variables and the point process is completely specified by its IIH. Such a process is called a *renewal* process, a definition motivated by the replacement of failed parts (such as light bulbs), each replacement of which forms a renewal of the point process.

The HPP, the DTMP, and the GRP are all renewal processes. The interevent-interval probability-density function for the HPP assumes the exponential form

$$p_\tau(\tau) = \lambda \, \exp(-\lambda \tau), \qquad (2)$$

where λ is the mean number of events per unit time. The interevent-interval mean and standard deviation are readily calculated to be $\langle \tau \rangle = 1/\lambda$ and $\sigma_\tau = 1/\lambda$, respectively, and the coefficient of variation (CV) is therefore $C \equiv \sigma_\tau / \langle \tau \rangle = 1$.

The interevent-interval probability-density function for the DTMP exhibits the same exponential form as that for the HPP but is truncated at short interevent intervals as a result of the dead time:

$$p_\tau(\tau) = \begin{cases} 0 & 0 \leq \tau < \tau_d \\ \lambda \, \exp[-\lambda(\tau - \tau_d)] & \tau \geq \tau_d, \end{cases} \quad (3)$$

where τ_d is the dead time and λ is the mean rate of the process before dead time is imposed. After the imposition of dead time the mean rate is

$$\mu = \frac{\lambda}{1 + \lambda \tau_d}. \qquad (4)$$

The interevent-interval mean and standard deviation are $\langle \tau \rangle = 1/\mu = \tau_d + 1/\lambda$ and $\sigma_\tau = 1/\lambda$, respectively, and the CV is $C = (1 + \lambda \tau_d)^{-1} < 1$. In the remainder of this paper the symbol μ is used to refer to the mean rate of an arbitrary point process; the symbol λ is usually reserved for the HPP.

The interevent-interval probability-density function for the GRP is the gamma distribution:

$$p_\tau(\tau) = \frac{(\mu r)^r \tau^{r-1} \exp(-\mu r \tau)}{\Gamma(r)}, \qquad \tau \geq 0, \qquad (5)$$

where μ is the mean rate, r is the order of the process, and $\Gamma(r) = \int_0^\infty x^{r-1} \exp(-x) dx$ is the gamma function evaluated at r. In general, r is not constrained to be an integer $(0 < r < \infty)$. The interevent-interval mean and standard deviation are $\langle \tau \rangle = 1/\mu$ and $\sigma_\tau = 1/\mu\sqrt{r}$, respectively, and the CV is $C = 1/\sqrt{r}$, which can be either less than or greater than unity depending on the value of r. For $r < 1$ $(r > 1)$ the gamma distribution is overdispersed (underdispersed) with respect to the exponential, for which $C = 1$. The GRP reduces to the HPP for the special case $r = 1$.

For nonrenewal processes, dependencies exist among the interevent intervals, and the IIH does not completely characterize the process. In that case measures that reveal the nature of the dependencies provide information that is complementary to that contained in the IIH. The sequence of action potentials in visual-system neurons falls in this class.

2. Rescaled Range Analysis
R/S provides information about correlations among blocks of interevent intervals. For a block of k interevent intervals, the difference between each interval and the mean interevent interval is obtained and successively added to a cumulative sum. The normalized range $R(k)$ is the difference between the maximum and minimum values that the cumulative sum attains, divided by the standard deviation of the interval size. $R(k)$ is plotted against k. Information about the nature and the degree of correlation in the process is obtained by fitting $R(k)$ to the function k^H, where H is the Hurst exponent.[52] For $H > 0.5$ positive correlation exists among the intervals, while $H < 0.5$ indicates the presence of negative correlation; $H = 0.5$ obtains for intervals with no correlation. For negatively correlated intervals, an interval that is larger than the mean tends, on average, to be preceded or followed by one smaller than the mean.

This widely used measure is generally assumed to be well suited to processes that exhibit long-term correlation or have a large variance,[52–55] but it appears not to be very robust since it exhibits large systematic errors and highly variable estimates of the Hurst coefficient for fractal-Gaussian-noise processes.[56] In any case, it appears not to have been used previously in visual-system spike-train analysis.

C. Event-Number Measures of a Point Process
It is advantageous to study some characteristics of a point process in terms of the sequence of event numbers (counts) $\{N_i\}$ rather than through the sequence of intervals $\{\tau_i\}$.[22,43,48,57]

Figure 2(c) illustrates how the sequence is obtained. The time axis is divided into equally spaced, contiguous time windows, each of duration T s, and the (integer) number of events in the ith window is counted and denoted N_i. This sequence $\{N_i\}$ forms a discrete-time random counting process of nonnegative integers. In general, information is lost in the transformation from the point process to the counting process, since the specific occurrence times of the events within each window are ignored. Nevertheless, for regular point processes, the information loss can be rendered arbitrarily small by the use of counting windows that are sufficiently short. Closely related to the sequence of counts is the sequence of rates (events/second) R_i, which is obtained by dividing each count N_i by the counting time T (this is the measure that is used in Fig. 1).

We employ a number of statistical measures to characterize the counting process $\{N_i\}$: the event-number histogram (ENH), the Fano factor (FF), the Allan factor (AF), and the event-number-based periodogram (PG). We also include the normalized coincidence rate (NCR) because of its important role in linking the other statistical measures.

1. Event-Number Histogram
Just as the IIH provides an estimate of the probability-density function of interevent-interval magnitude, the ENH $p_N(N; T)$ provides an estimate of the probability-mass function of the number of events N occurring in a time window of length T. Construction of the ENH, like

the IIH, involves loss of information, in this case the ordering of the counts. However, whereas the time scale of information contained in the IIH is the interevent interval, which is intrinsic to the process under consideration, the ENH reflects behavior occurring on the time scale of the counting time T. Since this time is externally specified by the observer, the character of the process at arbitrary time scales, including those spanning multiple interevent intervals, can be examined by the use of this measure.[22] For the HPP the probability-mass function is the simple Poisson distribution

$$p_N(N; T) = \frac{(\lambda T)^N \exp(-\lambda T)}{N!}. \tag{6}$$

The event-number distribution for the DTMP[51] is considerably more complex than Eq. (6) because the possible overlap of a dead-time interval across the boundary of adjacent counting windows results in correlation between the numbers of events in these intervals. As a result, the counts $\{N_i\}$ are no longer independent, though they become approximately so for counting times much greater than the dead-time interval. In this limit the probability-mass function approaches Gaussian form.[57]

The exact probability-mass function for the GRP is similarly complex, but the central limit theorem again provides a simple approximation for large values of T:

$$p_N(N; T) \cong \sqrt{\frac{r}{2\pi\mu T}} \exp\left[\frac{-r}{2\mu T}(N - \mu T)^2\right]. \tag{7}$$

Additional information pertaining to a point process can also be revealed by particular characteristics of the ENH. For example, a sawtoothlike form for the ENH, revealing higher probabilities for even than for odd numbers in a counting time T, implies that events tend to occur in pairs separated by less than T s.

The moments of the ENH, such as the event-number variance and mean, and their ratio, provide succinct and useful information about the process, as sketched in Subsection 3.C.2.

2. Fano Factor and Rate Standard Deviation
The FF, $F(T)$, is defined as the event-number variance divided by the event-number mean, which is a function of the counting time T:

$$F(T) = \frac{\mathrm{var}[N_i(T)]}{\langle N_i(T)\rangle}. \tag{8}$$

This quantity provides an abbreviated way of describing correlation in a sequence of events. It indicates the degree of event clustering or anticlustering in a point process relative to the benchmark HPP, for which $F(T) = 1$ for all T. This latter result is readily derived by calculating the count mean $\langle N_i(T)\rangle$ and the count variance $\mathrm{var}[N_i(T)]$, which, with the help of Eq. (6) for the Poisson distribution, leads to

$$\mathrm{var}[N_i(T)] = \langle N_i(T)\rangle = \lambda T. \tag{9}$$

Thus $F(T) = 1$ for all counting times T for the HPP.

In fact, the FF must approach unity at sufficiently small values of the counting time T for *any* regular point process because only zero or one event can be registered

in an arbitrarily short counting window for such a process. The sequence of counts then becomes a sequence of Bernoulli random variables, with a value of 0 or 1, and with a mean event number equal to the probability p of observing an event in the counting window. The variance of the Bernoulli distribution is simply $p(1 - p)$, so that

$$\lim_{T \to 0} F(T) = \lim_{T \to 0} \frac{p(1 - p)}{p} = 1, \qquad (10)$$

since $p \to 0$ as $T \to 0$.

For the DTMP the dead time imposes anticlustering (more regularity) on the point process for all but the shortest counting times. This anticlustering reduces the variance relative to the mean, which suppresses $F(T)$ so that it lies below unity. The asymptotic result for a HPP subject to nonparalyzable fixed dead time, valid in the limit of large T, is[58]

$$\lim_{T \to \infty} F(T) = (1 - \mu \tau_d)^2 = (1 + \lambda \tau_d)^{-2}, \qquad (11)$$

where μ and λ represent the post- and pre-dead-time event rates, respectively. When $\lambda \tau_d$ is appreciable, the imposition of dead time produces a nearly periodic series of events since one is always available immediately after the termination of the dead-time interval. The process is therefore anticlustered relative to the HPP and, as a consequence, has lower count variance and FF.

The GRP may be either less clustered or more clustered than the HPP, depending on the order r of the process. The asymptotic result, valid in the limit of large T, is

$$\lim_{T \to \infty} F(T) = \frac{1}{r}. \qquad (12)$$

In general, a FF less than unity indicates that a point process is more regular than the HPP at the particular time scale T, whereas an excess over unity indicates increased clustering at the given time scale.[22,23,48] This measure is sometimes called the index of dispersion; it appears to have been first used by Fano[59] in 1947 for characterizing the statistical fluctuations of the number of ions generated by individual fast charged particles.

For a FSPP, the FF assumes the power-law form T^α ($0 < \alpha \leq 1$) for large T. The parameter α is defined as the fractal exponent (or the scaling exponent) of the point process. The fractal exponent is ambiguously related to the Hurst exponent H, since some authors have used the quantity H to index fractal Gaussian noise (FGN) whereas others have used the same value of H to index the integral of FGN [which is fractional Brownian motion (FBM)].[56] The relationship between the quantities is $\alpha = 2H - 1$ for FGN and $\alpha = 2H + 1$ for FBM. We avoid this ambiguity by using α rather than H.

There are several measures that are equivalent to the FF: These include the variance–time curve,[48] relative dispersional analysis,[55] and the rate standard deviation (RSD) versus counting time.[60] The connection between the RSD and the FF is made by the use of $R_i = N_i/T$, where N_i is the number of spikes in the ith window (of duration T) and R_i is the local firing rate. The mean fir-

ing rate is then $\langle R_i(T) \rangle = \langle N_i(T) \rangle/T \equiv \mu$, and $\text{var}[R_i(T)] = \text{var}[N_i(T)]/T^2$, so that

$$F(T) = \frac{\text{var}[N_i(T)]}{\langle N_i \rangle} = \frac{T \, \text{var}[R_i(T)]}{\langle R_i \rangle} = \frac{T \sigma_R^2}{\langle R_i \rangle},$$

where σ_R is the standard deviation of the rate.

For a FSPP the FF assumes the power-law form T^α ($0 < \alpha \leq 1$), so that

$$\sigma_R(T) = \left[\frac{\mu F(T)}{T} \right]^{1/2} \propto \frac{1}{T^{(1-\alpha)/2}}.$$

For a nonfractal process $\alpha = 0$, so that the standard deviation of the rate is proportional to $1/\sqrt{T}$; the rate then converges relatively quickly as the averaging time increases, as illustrated in Fig. 1(b). The slower power-law convergence, illustrated in Fig. 1(a), results from the fractal nature of the neural spike-train data ($\alpha > 0$).

3. Allan Factor

Though the FF can detect the presence of self-similarity even when it cannot be discerned in a visual representation of a sequence of events, mathematical constraints prevent it from increasing with counting time faster than $\sim T^1$. It therefore provides a suitable measure only for fractal exponents in the range $0 < \alpha < 1$.[31,61]

The estimation of a fractal exponent that assumes a value greater than unity requires the use of a measure whose increase is not constrained in this way. In this subsection we define a measure called the Allan factor (AF), which is the ratio of the event-number Allan variance to twice the mean:

$$A(T) = \frac{\langle [N_{i+1}(T) - N_i(T)]^2 \rangle}{2 \langle N_i(T) \rangle}. \qquad (13)$$

The Allan variance is defined in terms of the variability of successive counts; it was first introduced in connection with the stability of atomic-based clocks.[62]

Like the FF, the AF is also a useful measure of the degree of event clustering (or anticlustering) in a point process relative to the benchmark HPP, for which $A(T) = 1$ for all T. In fact, for any point process, the AF is simply related to the FF by[31]

$$A(T) = 2F(T) - F(2T), \qquad (14)$$

so that, in general, both quantities vary with the counting time T. For a FSPP, the AF exhibits a power-law dependence that varies with the counting time T as $A(T) \sim T^\gamma$ ($0 < \gamma < 3$); it can rise as fast as $\sim T^3$ and can therefore be used to estimate fractal exponents over the expanded range $0 < \gamma < 3$.

For a FSPP with $0 < \alpha < 1$ the FF and the AF both vary as $\sim T^\alpha$, with the same fractal exponent $\gamma = \alpha$, over a large range of counting times T. Thus a doubly logarithmic plot of the AF for such a process will yield an estimate γ of the fractal exponent that is similar to the estimate α obtained from the FF.

For an arbitrary process, Eq. (14) shows that the asymptotic formula for the AF, valid in the limit of large T, is identical to that for the FF: $\lim_{T \to \infty} A(T) = \lim_{T \to \infty} F(T)$. In particular, for a DTMP with non-

paralyzable fixed dead time, we have $\lim_{T\to\infty} A(T)$ $= (1 + \lambda\tau_d)^{-2}$. Similarly, the asymptotic AF for the GRP for large T becomes

$$\lim_{T\to\infty} A(T) = \frac{1}{r}. \qquad (15)$$

Wavelet-based measures can also be used for estimating the fractal exponent of a point process.[61] The wavelet Fano factor (WFF) and the wavelet Allan factor (WAF) serve in this capacity as natural generalizations of the FF and the AF, respectively. This has been explicitly demonstrated for a LGN neural spike train.[61]

4. Periodogram

Fourier-transform methods provide another avenue for quantifying correlation in a point process. The PG is an estimate of the power spectral density (PSD) of a point process, revealing how the power is concentrated across frequency. The count-based PG is obtained by dividing a data set into contiguous segments of equal length $\mathscr{T}$. Within each segment, a discrete-index sequence $\{W_i\}$ is formed by further dividing $\mathscr{T}$ into M equal bins and then counting the number of events within each bin. A PG is then formed for each of the segments according to

$$S_{\text{segment}}(f) \equiv \frac{1}{M}|\widetilde{W}(f)|^2, \qquad (16)$$

where $\widetilde{W}(f)$ is the discrete Fourier transform (DFT) of the sequence $\{W_i\}$, and M is the length of the DFT.[63] All of the segment PG's are averaged together to form the final averaged PG, $S(f)$, which estimates the PSD in the frequency range from $1/\mathscr{T}$ to $M/2\mathscr{T}$ Hz. The count-based PG, as opposed to the interval-based PG, provides direct undistorted information about the time correlation of the underlying point process because the count index increases by unity every $\mathscr{T}/M$ s, in proportion to the real time of the point process.[43] In the special case in which the bin width $\mathscr{T}/M$ is short in comparison with the mean interevent interval $\langle\tau\rangle$, the count-based PG essentially reduces to the PG of the point process itself, since every bin contains either 0 or 1 event, to good approximation. For simplicity, we omit the dc power $S(0) = \mu^2$ arising from the constant term in the coincidence rate.

The PSD of a renewal process approaches μ at high frequencies and $\mu C^2 = \sigma_\tau^2/\langle\tau\rangle^3$ at low frequencies.[64] For the HPP, the PSD of the point process simply assumes the value of the mean firing rate λ across all nonzero frequencies. For the DTMP, the point-process PSD asymptotically approaches the following limits, at low and at high frequencies, respectively[64–66]:

$$S(f) = \begin{cases} \dfrac{\lambda}{(1 + \lambda\tau_d)^3} & \text{for } f \to 0 \\[2mm] \dfrac{\lambda}{1 + \lambda\tau_d} & \text{for } f \to \infty \end{cases}; \qquad (17)$$

at intermediate frequencies $S(f)$ exhibits oscillations of period τ_d that decay as the frequency increases.[67]

When we use the general form for the PSD of a renewal process,[65] $S(f) = \mu\,\mathrm{Re}([1 + \phi(f)]/[1 - \phi(f)])$, together with the interevent-interval characteristic func-

tion for the GRP,[67,68] $\phi(f) = (1 + j2\pi f/\mu r)^{-r}$, the point-process PSD for the GRP becomes

$$S(f) = \mu\,\mathrm{Re}\left[\frac{(1 + j2\pi f/\mu r)^r + 1}{(1 + j2\pi f/\mu r)^r - 1}\right], \qquad (18)$$

where $\mathrm{Re}(Z)$ represents the real part of the complex quantity Z.

For a FSPP, the PSD decreases as a power-law function of the frequency f, so that $S(f) \sim f^{-\beta}$ over some range of low frequencies.[23] The fractal exponent β estimated from the PG assumes a value similar to that of γ when $0 < \beta < 3$ and similar to that of γ and α when $0 < \beta < 1$. Unlike the FF and the AF, the fractal exponent obtained from the PG has no upper bound.

5. Normalized Coincidence Rate

The normalized coincidence rate (NCR) plays the role of the correlation function for point processes. Although it is difficult to estimate this quantity reliably for finite data segments (because of the sparseness of data in short counting windows), we introduce it because of the underlying role that it plays in the theory of stochastic point processes. Specifically, it is directly related to the FF (and thereby the RSD), the AF, and the PSD of the point process.

The NCR, $g^{(2)}(\tau)$, is defined as[27,28,48]

$$g^{(2)}(\tau)$$
$$\equiv \frac{\Pr[\mathscr{E}(t, t + dt) \quad \text{and} \quad \mathscr{E}(t + \tau, t + \tau + dt)]}{\Pr[\mathscr{E}(t, t + dt)]\Pr[\mathscr{E}(t + \tau, t + \tau + dt)]}, \qquad (19)$$

where $\mathscr{E}(x, y)$ denotes the occurrence of an event in the interval (x, y) and τ is a delay time. The NCR is sometimes called the autocorrelogram. For a HPP, $g^{(2)}(\tau) = 1$ for all τ.

The FF, $F(T)$, and the NCR, $g^{(2)}(\tau)$, enjoy a unique relation for an *arbitrary* stationary point process[23,27,28,48]:

$$F(T) = 1 + \frac{2\mu}{T}\int_0^T (T - \tau)[g^{(2)}(\tau) - 1]d\tau \qquad (20a)$$

and, conversely,

$$g^{(2)}(\tau) = 1 + \frac{1}{2\mu}\frac{\partial^2}{\partial T^2}[TF(T)]|_{T=\tau}, \qquad (20b)$$

where again μ is the mean rate of the point process. The relationship between the AF, $A(T)$, and $g^{(2)}(\tau)$ follows from the use of Eq. (20a) in conjunction with Eq. (14).

The PSD of a stochastic point process is the Fourier transform of the NCR, in the same way that the PSD and the autocorrelation function of a continuous stochastic process form a Fourier-transform pair. The count-based PSD is a filtered and periodic version of the point-process-based PSD.

For FSPP's, a power-law dependence of the form $F(T) \sim T^\alpha$ $(0 < \alpha < 1)$ in the long-counting-time limit implies that the underlying point process has a power-law NCR $g^{(2)}(\tau) \sim |\tau|^{\alpha-1}$ and, as indicated in Subsection 3.C.4, a PSD that behaves as $S(f) \sim f^{-\alpha}$.[23,27,28,31,35] Although the correlation between a single pair of events is

typically rather small for FSPP's, Eq. (20a) illustrates that the values of $F(T)$ and $A(T)$ at a particular counting time T can become quite large because the FF and the AF integrate the many correlations from different pairs of events within the counting window T. As a result, even weak correlation in $g^{(2)}(\tau)$ can lead to dramatic departures of the FF and the AF from unity.[27,28]

D.   Analysis of Surrogate Data

Complementary information relating to the character and the origin of the fractal fluctuations in visual-system nerve-spike trains may be obtained by applying the various statistical measures discussed above to surrogate data sets. These are point processes constructed from the original sequence of action potentials in ways designed to preserve certain characteristics of the original data while eliminating (or modifying) others. Surrogate data analysis provides a way of determining whether a given observation arises from a particular property of the data set.

In this paper we make use of only one kind of surrogate data set: shuffled intervals[43]; other kinds of surrogate data analysis are discussed elsewhere.[43] In particular, we compare statistical measures calculated from both the original data and its shuffled surrogate to distinguish those properties of the data that arise from correlation among intervals (such as from long-term rate fluctuations) from those properties inherent in the form of the IIH.

The shuffled surrogate data set is formed by randomly reordering the sequence of interevent intervals $\{\tau_i\}$ of the original data set. Such random reordering destroys dependencies among the intervals, and therefore the long-term correlation properties of the data, while exactly preserving the IIH. It provides a method for generating a point process that is essentially renewal in nature, with an IIH that is identical to that of the original point process. Data set MD2-LGN and its shuffled version were used to generate Figs. 1(a) and 1(b), respectively.

4.   RESULTS

A.   Fractal Character of Retinal-Ganglion-Cell and Lateral-Geniculate-Cell Neural Spike Trains

The interevent-interval and event-number measures described in Section 3 were applied to maintained-discharge spike trains recorded from LGN relay neurons in the anesthetized and paralyzed cat. This preparation permits pre- and post-synaptic activity to be reliably distinguished, so that RGC and LGN activity can be simultaneously collected and directly compared. All of the spike trains studied were behaving in a tonic mode.

Retinal afferent activity manifested in the thalamus takes the form of slow synaptic (S) potentials, also called pre-potentials.[69–73] It has now been firmly established that (1) every action potential in a retinal afferent fiber elicits an S potential in the LGN,[71] (2) all S potentials observed in the LGN arise from the activity of RGC's,[73] and (3) most LGN principal cells receive the bulk of their excitatory input from a single RGC.[71,74] These observations make it possible to compare quantitatively the input

and the output of a particular LGN neuron by simultaneously monitoring its S potentials and action potentials.

The 26 data sets examined here are drawn from 13 relay neurons, each yielding a pair (input and output) of spike trains. We characterized eight of these neurons as X-ON cells, four as X-OFF cells, and one as a Y-ON cell. Selected characteristics of these data sets are provided in Tables 1 and 2. The adapting luminance of the stimulus was fixed at 0, 6.5, 33, or 65 cd/m^2 (see Tables 1 and 2).

The mean firing rates displayed in Tables 1 and 2 show that the spike rates observed at the LGN outputs are, on average, only 25% of the input RGC rates, although this percentage varies significantly across the data sets that we examine. It has been determined previously that this ratio depends on a number of factors,[75] including the contrast of the stimulus.[76] LGN cells typically (but not always) exhibit larger values of the CV than RGC's; it has been noted previously that the CV is usually inversely related to the firing rate, at least for RGC's.[6,13,15]

The pairs of data sets (MD2-RET and MD2-LGN) used for purposes of illustration in this paper are typical of their respective classes of data.

In Fig. 3 we present IIH's for RGC and LGN spike trains simultaneously obtained from cell MD2 (solid curves). Since random reordering of the intervals does not alter the relative frequency with which they occur, the IIH's of the shuffled surrogates are the same as those of the original data sets. Also shown are the respective best-fitting results for the GRP (dotted) model and the DTMP (dashed) model with fixed nonparalyzable dead time. The DTMP parameters λ and τ_d were estimated by finding the least-squares fit of Eq. (3) to the experimental IIH. The GRP probability-density function in Eq. (5) was obtained by equating its first and second moments to the experimental values (μ was set to $1/\langle\tau\rangle$, and r was set to $1/C^2$). The GRP is seen to provide a good fit to the IIH for the RGC, while the DTMP with fixed dead time clearly does not. We have shown previously, however, that incorporating stochastic,[10] or relative,[77] refractoriness in the DTMP provides an excellent fit to the IIH provided that $C < 1$, as is generally the case for the maintained, non-dark discharge.

Neither the GRP nor the DTMP proves suitable for modeling the LGN IIH at short interevent times, as is clear from Fig. 3(b). A superior representation is provided by the refractoriness-modified shot-noise-driven doubly stochastic Poisson process (RM-SNDP).[11,14] This has been explicitly demonstrated for the RGC dark-discharge IIH,[11,14] which often exhibits $C > 1$ and closely resembles the LGN IIH illustrated in Fig. 3(b). With appropriate choices for the multiplicative behavior and the refractoriness recovery, the RM-SNDP can accommodate data for $C < 1$ as well. Further discussion regarding the relevance of this model to the problem at hand is left to the discussion in Section 6.

A rescaled range analysis (R/S) for the two data sets and their shuffled surrogates is presented in Fig. 4. The dotted curves represent the baseline function $\sqrt{k}$, corresponding to uncorrelated interevent intervals. Positive correlation among intervals (nonrenewal behavior) is present in both cases, since $R(k)$ grows more rapidly than $\sqrt{k}$. This measure fails to reveal any substantial differ-

Table 1. Characteristics of the Retinal-Ganglion-Cell Recordings

File Name	Cell Type	Number of Intervals	Duration of Data (s)	Luminance Level (cd/m^2)	Mean Rate μ (s^{-1})	Mean Interval $\langle\tau\rangle$ (s)	Interval Std. Dev. σ_τ (s)	Interval CV C	FF Exponent α	AF Exponent γ	PG Exponent β
MD1-RET	X-ON	61,500	2500	33	24.6	0.0406	0.028	0.6906	0.82	0.88	1.32
MD2-RET	X-ON	140,432	6388	33	22.0	0.0455	0.028	0.6223	0.56	0.48	0.33
MD6-RET	Y-ON	126,276	3901	33	32.4	0.0309	0.016	0.5125	0.69	0.94	0.99
MDS-RET	X-ON	56,661	3226	33	17.6	0.0569	0.066	0.7715	0.82	1.13	0.93
Y0101RET	X-ON	201,496	5088	65	39.6	0.0253	0.011	0.4382	0.39	0.49	0.73
Y0102REF	X-ON	161,301	5127	6.5	31.5	0.0318	0.015	0.4823	0.32	0.68	1.00
Y0103REF	X-ON	36,502	4960	0	7.4	0.1359	0.207	1.5214	1.00	1.57	0.56
Y0202REF	X-ON	130,173	4384	65	29.7	0.0337	0.025	0.7432	0.99	1.63	1.50
Y0203REF	X-ON	38,841	4965	0	7.8	0.1279	0.349	2.7273	0.86	1.94	2.00
Y1102REF	X-OFF	47,732	5127	6.5	9.3	0.1074	0.134	1.2474	0.81	0.90	1.41
Y1103REF	X-OFF	234,096	4962	0	47.2	0.0212	0.017	0.8197	0.78	1.23	0.97
Y1202REF	X-OFF	206,627	4384	65	47.1	0.0212	0.014	0.6795	0.92	1.89	1.94
Y1203REF	X-OFF	116,470	5040	0	23.1	0.0433	0.058	1.3359	0.96	2.16	1.69
Mean		119,854	4619		26.1	0.0555	0.074	0.9686	0.76	1.22	1.18
Std. dev.					13.6	0.0406	0.101	0.6278	0.22	0.56	0.51

Table 2. Characteristics of the Lateral-Geniculate-Cell Recordings

File Name	Cell Type	Number of Intervals	Duration of Data (s)	Luminance Level (cd/m^2)	Mean Rate μ (s^{-1})	Mean Interval $\langle\tau\rangle$ (s)	Interval Std. Dev. σ_τ (s)	Interval CV C	FF Exponent α	AF Exponent γ	PG Exponent β
MD1-LGN	X-ON	1688	2500	33	6.8	0.1481	0.167	1.1271	0.37	0.33	0.70
MD2-LGN	X-ON	70,320	6388	33	11.0	0.0908	0.305	1.0268	0.34	0.38	0.46
MD6-LGN	Y-ON	33,890	3901	33	8.7	0.1150	0.147	1.2821	0.84	1.26	1.66
MDS-LGN	X-ON	24,285	3226	33	7.5	0.1328	0.197	1.4824	0.56	0.63	0.80
Y0101LGN	X-ON	22,852	5088	65	4.5	0.2227	0.255	1.1469	0.37	0.43	0.56
Y0102LGN	X-ON	31,878	5127	6.5	6.2	0.1608	0.189	1.1750	0.78	0.53	0.48
Y0103LGN	X-ON	25,234	4960	0	5.1	0.1966	0.533	1.4425	1.00	1.27	0.19
Y0202LGN	X-ON	18,376	4384	65	4.2	0.2385	0.401	1.6808	0.49	0.67	1.21
Y0203LGN	X-ON	29,265	4965	0	5.9	0.1696	0.471	2.7800	0.92	1.86	1.62
Y1102LGN	X-OFF	27,734	5127	6.5	5.4	0.1848	0.220	1.1855	0.39	0.63	1.06
Y1103LGN	X-OFF	79,453	4962	0	16.0	0.0624	0.064	1.0190	0.70	0.38	0.29
Y1202LGN	X-OFF	5338	4384	65	1.2	0.8200	1.29	1.5728	0.83	1.10	1.22
Y1203LGN	X-OFF	18,297	5040	0	3.6	0.2754	0.439	1.5953	0.68	1.76	1.85
Mean		29893	4619		6.6	0.2167	0.360	1.4243	0.64	0.86	0.93
Std. dev.					3.7	0.1907	0.312	0.4642	0.23	0.53	0.55

ence between the RGC and LGN data, however. R/S curves for the shuffled surrogate data sets [lower solid curves in Figs. 4(a) and 4(b)] display a dependence quite close to $\sqrt{k}$, as expected for renewal point processes.[52–56]

The ENH's for the same RGC and LGN data sets, generated with a counting time of $T = 1.0$ s, are shown as the solid curves in Figs. 5(a) and 5(b), respectively. Aside from the difference in mean values (the firing rate of this particular RGC is 22 s^{-1}, whereas that of its target LGN cell is 11 s^{-1}), the curves are quite similar in appearance. The ENH for the RGC can be approximated by the DTMP counting distribution (its variance lies below the mean at this counting time),[10,51] whereas the ENH for the LGN cell can be approximated by the Neyman Type-A distribu-

tion (its variance exceeds the mean at this counting time).[14] Shuffling the data narrows the ENH's (dotted curves), which reflects reduced count variance. This indicates that the count variance of the original process arises at least in part from the ordering of the intervals, which accords with the serial dependence shown in Fig. 4. ENH's for those GRP's that best fit the shuffled-surrogate ENH's are indicated by dashed curves. The renewal ENH's (dotted and dashed curves) are Gaussian-like, as expected from renewal theory.[48,57,68]

FF's for the same RGC and LGN data sets are shown (on doubly logarithmic coordinates) as the solid curves in Figs. 6(a) and 6(b), respectively. The dotted curves represent average FF's calculated from ten independent
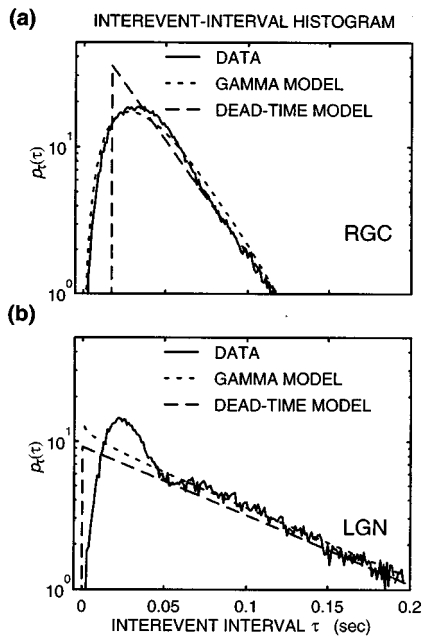
Fig. 3. Semilogarithmic plots of the interevent-interval histograms (IIH's) for retinal-ganglion-cell (RGC) and lateral-geniculate-nucleus (LGN) nerve-spike trains (file names MD2-RET and MD2-LGN, respectively). The spike trains were simultaneously obtained from the same LGN relay neuron. The histograms were normalized to have unit area. Also shown are IIH's for two candidate models (dotted and dashed curves). (a) IIH for the RGC data (solid curve), along with the best-fitting theoretical curve for the gamma-renewal-process (GRP) model (dotted curve) and for the fixed-dead-time-modified Poisson process (DTMP) model (dashed curve). The GRP model provides a good fit to the IIH. (b) IIH for the LGN data (solid curve), along with the best-fitting theoretical curve for the GRP model (dotted curve) and for the DTMP model (dashed curve). Neither of these two models provides a particularly good fit for short times, but both do well at longer times.

shufflings of the data; the light gray shading indicates the region bounded by ± 1 standard deviation about the mean of the shuffled curves. The values of the FF's for the shuffled data sets remain close to unity, providing further evidence that the shuffling process destroys the long-term positive correlation in the data. The short horizontal bars at the right-hand ordinates represent asymptotic values for the best-fitting GRP models, for which $F(T \to \infty) = C^2$ (this relationship is satisfied for all renewal processes). Dashed lines with unity slope, for which $F(T) \propto T$, are shown for visual comparison with the data.

For short counting times ($T \to 0$) the FF's approach unity, in accordance with Eq. (10). For time scales over which the underlying events are highly regular, and thereby exhibit low variance, the FF dips well below unity. For counting times greater than approximately 1 s, the FF's increases above unity and grow approximately as T^α. This indicates that the data exhibit power-law correlation and fractal behavior over the corresponding time scales. The onset of this power-law behavior occurs when the counting window is sufficiently large to allow fractal event clustering to overcome the anticlustering imposed by refractoriness. Estimates of α are provided in Tables 1 and 2 for all data sets.

The limited amount of spike-count mean and variance data that we have been able to find in the literature is in rough agreement with our results. Barlow and Levick,[6] for example, collected two maintained- (dark-) discharge ENH's (see Figure 5 on page 707 of their paper), using $T = 0.1$ and 1 s. Values of the FF extracted from their data are similar to the values we observe.

The AF's presented in Fig. 7 (solid curves) have features similar to those of the FF's and, for the most part, share the same underlying explanations. For counting times greater than approximately 1 s, the AF's grow approximately as T^γ. There is an important distinction that ultimately renders the AF more suitable than the FF for estimating the fractal exponent of a nerve-spike train: the power-law exponent γ has a larger range than α. Indeed, the exponents estimated by use of the AF frequently exceed unity for RGC and LGN spike trains (see Tables 1 and 2).

In Figs. 8(a) and 8(b) we present the averaged PG's, $S(f)$, for the same RGC and LGN data sets, on doubly logarithmic coordinates (solid curves). Count-based PG's were formed by dividing the data sets into contiguous segments of equal length $\mathcal{T} = 250$ s. Each of these seg-
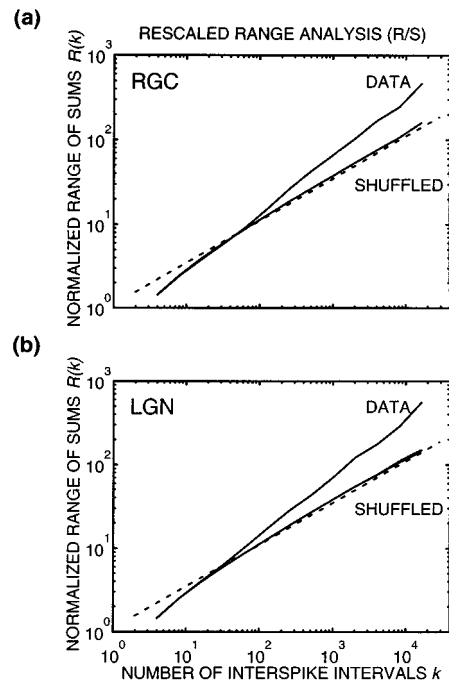

Fig. 4. Rescaled range analysis (R/S) for the same data sets as those analyzed in Fig. 3 and for shuffled surrogates of the data. (a) R/S plot for the RGC data (upper solid curve) along with the mean of ten R/S curves generated by independent shufflings of the original data set (lower solid curve). The standard deviation of the surrogate R/S curve is not shown, since it is less than the thickness of the curve. (b) R/S plot for the LGN data (upper solid curve) along with the mean of ten R/S curves generated by independent shufflings (lower solid curve). The standard deviation of the surrogate R/S curve is again not shown because of its small value. In both (a) and (b), for sufficiently large k, the R/S curves have a slope greater than 0.5 on this doubly logarithmic plot, indicating the presence of positive correlation. The shuffled-surrogate curves have a dependence very close to $\sqrt{k}$ (dotted curves), as expected for sequences of random variables that are essentially independent.
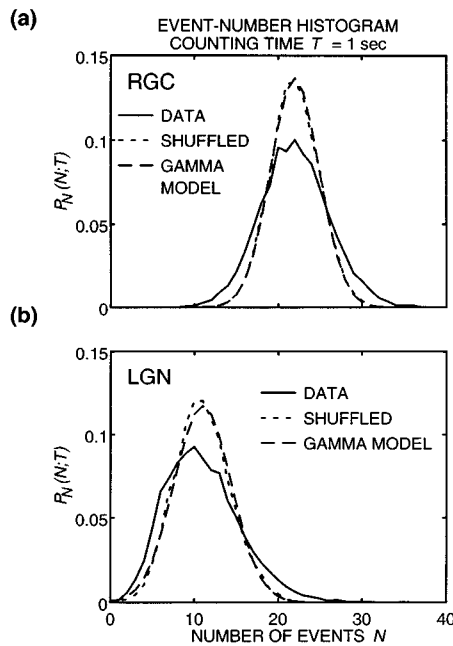
Fig. 5. Event-number histograms (ENH's) for the same data sets as those analyzed in Figs. 3 and 4, with the use of a counting time of $T = 1.0$ s, shown together with the same measures for shuffled surrogates of the data and their best-fitting GRP ENH's. The RGC [solid curve in (a)] and LGN [solid curve in (b)] histograms were normalized so that they summed to unity. The original ENH's in (a) and (b) are wider than the shuffled and model ENH's, revealing their greater count variances on this time scale and indicating the presence of long-duration correlation in the original sequence of interevent intervals. For these particular data sets the firing rate of the RGC is approximately twice that of its target LGN cell.

ments was further divided into $M = 32,768$ equal bins, so that the bin width was $\mathcal{T}/M = 7.6$ ms. A PG for each segment was then formed in accordance with Eq. (16), and the final estimate of the PSD (in the frequency range from $1/\mathcal{T} = 0.004$ to $M/2\mathcal{T} = 66$ Hz) was obtained by averaging these PG's. Because the bin width is short in comparison with the mean interspike interval $\langle \tau \rangle$ for both the RGC and LGN spike trains, there is rarely more than a single event in any bin and the calculated result is essentially the PSD estimate of the point process itself.

The dotted curves in Fig. 8 represent the PG's calculated from shuffled surrogates of the data sets. After shuffling, the PG's are flat at low frequencies, indicating that the counts are uncorrelated, as expected for a renewal process when $f \ll 1/\langle \tau \rangle$. The white curves through the centers of the PG's are theoretical PSD's for the GRP model [given by Eq. (18)], using parameters that best fit the IIH's of the data sets. The original data are satisfactorily modeled by the renewal theory for frequencies above approximately 0.5 Hz. In this same frequency range our PG's behave quite similarly to the PSD estimates obtained by Robson and Troy[15,16] for RGC spike trains. The Fourier components of RGC and LGN spike trains appear to have been first examined by Derrington and Lennie[78] and by Troy,[18] respectively.

The behavior of the unshuffled data (solid curves) at low frequencies (<0.5 Hz) indicates the presence of long-

duration correlation in the spike trains. The PG's are satisfactorily approximated by power-law functions of the form $S(f) \propto f^{-\beta}$ over a substantial range of low frequencies. The decreasing power-law behavior of the PG's evident in Fig. 8 is consistent with the power-law growth of the FF's and the AF's at large counting times, represented in Figs. 6 and 7, respectively, and with the self-similarity of the rate fluctuations revealed in Fig. 1(a).[23,27,28,61] Indeed, the values of β and γ are significantly correlated [correlation coefficient $\rho = 0.71$ ($p < 0.015$)] for both the RGC and the LGN data. The dashed lines in Fig. 8, shown for visual comparison, represent $1/f$-type behavior. Spectral estimates at low frequencies could not be examined by Robson and Troy[15,16] because they divided their data into short segments of duration $\mathcal{T} = 2.048$ s (see the discussion in Subsection 4.B below).

B. Data Selection: Dilution of Fractal Behavior
Researchers often select specific short segments of data to eliminate putative nonstationarities. In their analysis of maintained-discharge LGN spike trains, for example, Troy[18] and Levine and Troy[21] chose a collection of 3.072-s data segments with mean rates that were approximately equal. However, the observation of fractal behavior requires long data sets, and at the very heart of such behavior are large fluctuations that take the form of spike bursts. Moreover, selecting a particular short segment of
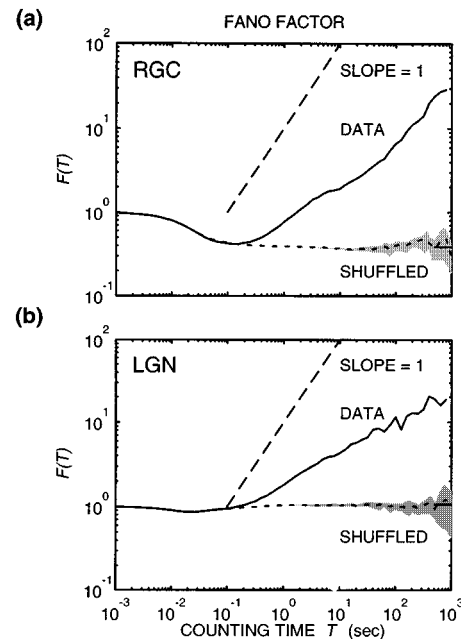

Fig. 6. Doubly logarithmic plots of the FF's (solid curves) for the same data sets as those analyzed in Figs. 3–5, along with the FF's for shuffled surrogates of the data (gray areas indicate the region bounded by ± 1 standard deviation about the mean of the set of ten shuffled FF's, represented by dotted curves), and asymptotic values of the FF's for the best-fitting GRP models (short horizontal bars at the right-hand ordinates). The FF's for the shuffled surrogates always lie near unity, indicating that long-duration correlation associated with the ordering of the intervals has been eliminated by the shuffling process, leaving only the correlation intrinsic to the form of the IIH. Dashed lines of unity slope [indicating $F(T) \propto T$] are included for comparison.
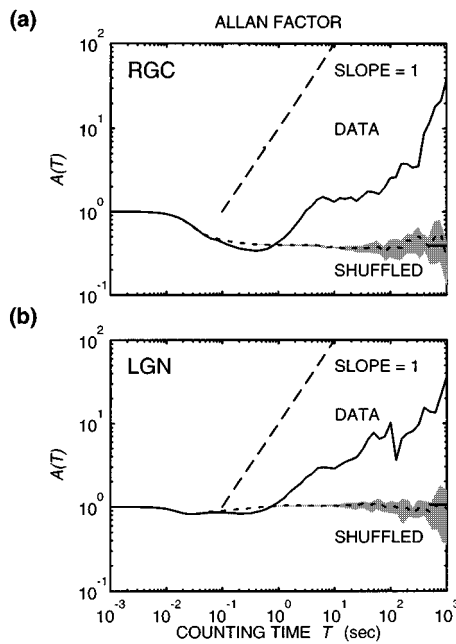
Fig. 7. Doubly logarithmic plots of the AF's (solid curves) for the same data sets as those analyzed in Figs. 3–6, along with the AF's for shuffled surrogates of the data (gray areas indicate the region bounded by ± 1 standard deviation about the mean of the set of ten shuffled AF's, represented by dotted curves), and asymptotic values of the AF's for the best-fitting GRP models (short horizontal bars at the right-hand ordinates). The AF's for the shuffled surrogates always lie near unity, indicating that long-duration correlation associated with the ordering of the intervals has been eliminated by the shuffling process, leaving only the correlation intrinsic to the form of the IIH. Dashed lines of unity slope [indicating $A(T) \propto T$] are included for comparison.

data on the basis of lack of variability (i.e., lack of burstiness or lack of changes in the mean) serves to reduce further the manifestations of fractal behavior.

For data segments of duration $\mathscr{T} = 3.072$ s, such as those chosen by Levine and Troy,[21] the lowest frequency available to the PG is $f_{\min} = 1/\mathscr{T} = 1/3.072 = 0.33$ Hz. The LGN PG presented in Fig. 8(b) reveals only a hint of fractal behavior at this frequency. In a similar vein, assuming that ten such segments are available to provide sufficient statistical accuracy, the maximum counting time available to the FF and the AF would be $T_{\max} = 3.072$ s. The FF in Fig. 6(b) and the AF in Fig. 7(b) do not provide convincing evidence for fractal behavior for counting times up to this value.

It is therefore quite possible that the LGN data examined by Troy[18] and by Levine and Troy[21] was indeed fractal, but that they removed most traces of such behavior by selecting short segments of data for analysis, and further by choosing precisely those data segments that exhibited minimal fluctuations. The RGC data sets collected by Troy and Robson[16] were divided into segments of duration $\mathscr{T} = 2.048$ s and therefore also suffer from this limitation.

C. Comparison of Fractal Exponents Derived from Retinal-Ganglion-Cell and Lateral-Geniculate-Cell Firing Patterns
All 26 of the RGC and LGN data sets that we investigated exhibit fractal behavior, as discussed in Subsection 4.A.

The fractal exponents of the RGC and LGN spike trains, estimated using the FF, the AF, and the PG, are displayed along the abscissas and the ordinates of Fig. 9. The spread in values is considerable, as is typical with fractal event sequences.[23,61]

It is apparent from Figs. 9(b) and 9(c) that the AF exponent γ and the PG exponent β both exceed unity for many RGC and LGN data sets. Since α is restricted to lie below unity [as it indeed does; see Fig. 9(a)], this confirms that the FF is not a useful measure for estimating the fractal exponents of many RGC and LGN data sets.

The plots presented in Figs. 9(b) and 9(c) relate the action-potential firing patterns at the outputs and the inputs of the LGN relay cells. The correlation coefficients turn out to be substantial: $\rho = 0.77$ ($p < 0.006$) and 0.73 ($p < 0.01$) for γ and β, respectively. Therefore, although the values of γ and β for any RGC data set can assume a large range of possible values (as shown in Table 1), the observed values of γ and β for its associated LGN data set will likely not differ significantly. Therefore, either the pattern of action-potential firings is partially transmitted from the RGC to the target LGN cell (or vice versa) or there is a common origin for the pair of firing patterns. On average, the fractal exponents of RGC spike trains are slightly larger than those of their target LGN cells. The difference is statistically significant (from the Student t test $p < 0.001$ for γ and β).
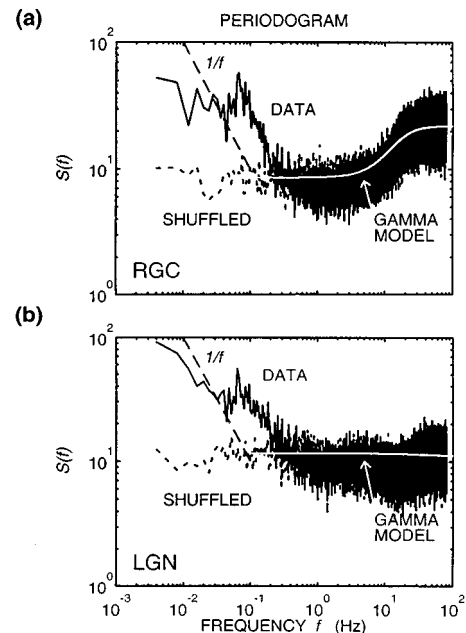

Fig. 8. Averaged PG's for the same spike trains as those analyzed in Figs. 3–7 (solid curves), presented on doubly logarithmic coordinates. The units on the ordinate are spikes squared per seconds squared per Hertz. The shuffled-surrogate PG's are shown as dotted curves. The high-frequency asymptote on the ordinate is numerically equal to the firing rate μ, whereas the low-frequency asymptote for the shuffled data (representing the renewal process) is numerically equal to μC^2. The PG's for the GRP with parameters that best fit the IIH's are shown as the white curves. The function $1/f$ is included for comparison (dashed curves).
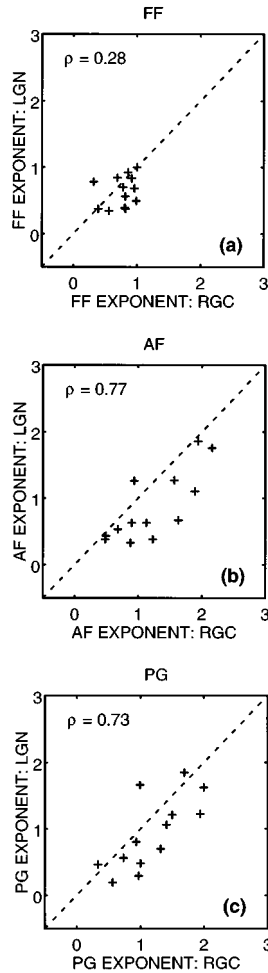
Fig. 9.   Estimates of the fractal exponents obtained from (a) the FF, (b) the AF, and (c) the PG.   In each plot the exponent estimated from the RGC spike train is plotted along the abscissa, while the exponent estimated from the LGN spike train is plotted along the ordinate.   The exponent associated with a given RGC spike train is significantly correlated with that of its target LGN spike train.

5. GAMMA-BASED FRACTAL DOUBLY STOCHASTIC POINT-PROCESS MODEL

Of the three simple renewal models discussed in Section 3 (HPP, DTMP, and GRP), the gamma-r point process best describes the IIH's of RGC and LGN spike trains.   However, it is clear that a FSPP is required to account for the fractal behavior inherent in the data.

   We construct a mathematical model that accords with both the short- and long-term features of the RGC and LGN spike trains by constructing a FSPP with the GRP as its core (see Fig. 10).   The model is endowed with long-duration correlation by imparting fractal fluctuations to the rate $\mu(t)$ of the GRP.   These rate fluctuations are taken to be fractal binomial noise (FBN),[23] which is describable as the sum of K iid alternating fractal renewal processes, as shown schematically in Fig. 10.   Each of the constituent processes assumes a value of 0 or a, and switches states at a time drawn from a power-law interevent-interval probability-density function.   FBN is useful for describing fractal ion-channel behavior and intracellular ionic concentrations.[23,38]

   Our FSPP may therefore be described as a fractal binomial-noise-driven doubly stochastic gamma (FBNDG) point process.   A special case of the FBNDG, the fractal binomial-noise-driven doubly stochastic Poisson point process (FBNDP), does an excellent job of describing the action-potential activity of primary afferent auditory-nerve fibers in a number of species, when refractoriness effects are included.[23,28,79]   The Poisson kernel with refractoriness modification is more suitable than the gamma kernel for this application because auditory-system IIH's behave more like the shifted exponential density in Eq. (3) than like the gamma density in Eq. (5).   Another related FSPP is the fractal lognormal-noise-driven doubly stochastic Poisson point process (FLNDP), which characterizes vesicular exocytosis in the developing neuromuscular junction.[39]   The FBNDP is also a special case of the FLNDP.

   FBNDG point processes are constructed by means of the following procedure.   A GRP is simulated by mapping interevent intervals u_i uniformly distributed between 0 and 1 into GRP-distributed intervals τ_i by means of the function $P(\tau_i) = u_i$, where $P(\tau)$ is the probability-distribution function for the GRP:

$$P(\tau) = \int_0^{\tau} p_{\tau}(t)\mathrm{d}t = \frac{(\mu r)^r}{\Gamma(r)} \int_0^{\tau} t^{r-1} \exp(-\mu r t)\mathrm{d}t$$

$$= \frac{1}{\Gamma(r)} \int_0^{\mu r \tau} \nu^{r-1}\exp(-\nu)\mathrm{d}\nu = \frac{\gamma(r, \mu r \tau)}{\Gamma(r)}. \quad (21)$$

$\gamma(r, \mu r \tau)$ is an incomplete gamma function that is readily evaluated by numerical integration.

   To model a given data set, we set the order r of the GRP kernel equal to $1/C^2$, where C is the measured interevent-interval CV.   FBN is simulated[23] using a mean rate $\langle \mu(t) \rangle$ (which is governed by the height a and the number K of constituent alternating fractal renewal processes) set equal to the mean firing rate of the data, μ.   The fractal onset time T_0 (determined by K and by cutoff
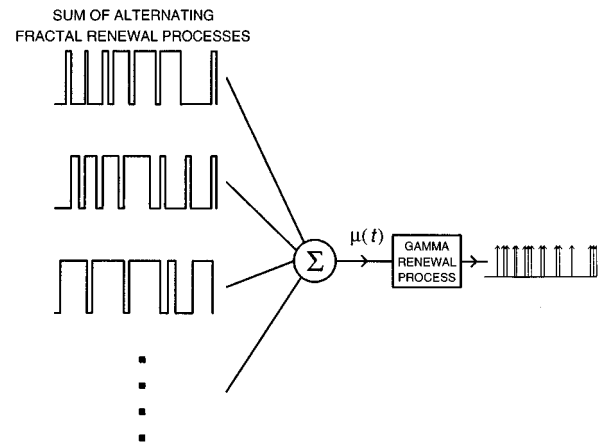

Fig. 10.   Construction of the fractal binomial-noise-driven doubly stochastic gamma-r process (FBNDG).   This model characterizes the statistical behavior of RGC and LGN spike trains remarkably well.   Fractal binomial noise (FBN), generated from the sum of K alternating fractal renewal processes, serves as the time-varying rate of a GRP with fixed order r.
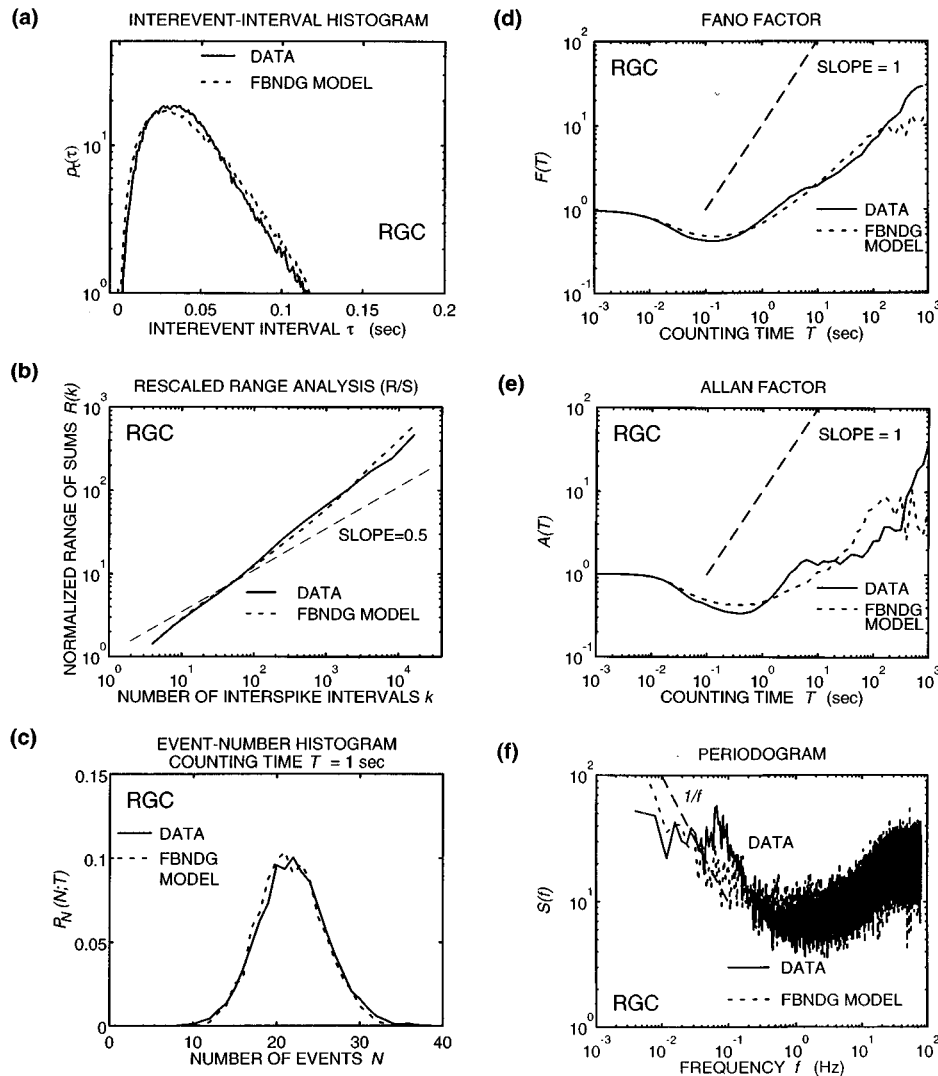
Fig. 11. Comparison of data presented in Figs. 3(a)–8(a) for RGC data set MD2-RET with the predictions of the FBNDG model illustrated in Fig. 10. The model uses four parameters drawn from the data: μ, C, α, and T_0. The FBNDG does just about as well as the GRP for (a) the IIH, and incomparably better for (b) R/S, (c) the ENH, (d) the FF, (e) the AF, and (f) the PG. Thus the FBNDG model preserves the IIH statistics of the original GRP model while accommodating the long-term correlations manifested in R/S and in the ENH, the FF, the AF, and the PG.

parameters of the constituent processes), and the fractal exponent of the FBN (determined by the fractal exponents α of the constituent processes), are set equal to the time at which the FF becomes proportional to T^α, and the measured exponent of the FF for the data, respectively. Thus the model makes use of four parameters drawn from the data: μ, C, α, and T_0. The fractal exponent can alternatively be based on the AF or the PG, which is desirable when γ or β is greater than unity.

The data presented in Figs. 3(a), 4(a), 5(a), 6(a), 7(a), and 8(a) for RGC data set MD2-RET are compared with the predictions of the FBNDG model in Figs. 11(a), 11(b), 11(c), 11(d), 11(e), and 11(f), respectively. The agreement is quite good for all measures investigated. In particular, the FBNDG does just about as well as the GRP for the IIH [compare Figs. 3(a) and 11(a)] and incomparably better for R/S [compare Figs. 4(a) and 11(b)], the ENH [compare Figs. 5(a) and 11(c)], the FF [compare Figs. 6(a) and 11(d)], the AF [compare Figs. 7(a) and 11(e)], and the

PG [compare Figs. 8(a) and 11(f)]. In short, the FBNDG model preserves the IIH statistics of the original GRP model while accommodating the fractal behavior observed in the various measures that we have reported in this paper.

6. DISCUSSION

A FBNDG model has been developed that imparts (nonrenewal) fractal fluctuations to a (renewal) gamma-distributed kernel. The overall result is a nonrenewal fractal stochastic point process. This serves quite well for characterizing the behavior of RGC and LGN spike trains over all time scales, as illustrated by the good fits to the data exhibited in Fig. 11. The FBNDG provides a reasonable model for all of the maintained-discharge (and dark-discharge) data sets that we have examined (see Tables 1 and 2).

A. Gamma Model for Short-Term Behavior

For many vision researchers the GRP has been the model of choice for describing short-term RGC and LGN spike statistics. The original motivation for considering the GRP in visual neurophysiology was the prospect that scaling might explain the large compression between the rate of quantal absorption and the rate of RGC nerve-spike generation[6]; a HPP scaled in such a way that only every rth event survives results in the GRP.[68] Unfortunately, this interpretation leads to a host of inconsistencies,[80] not the least of which is that the parameters turn out to be quite wrong.[6,10]

Nevertheless, the GRP has continued to be used for modeling short-term spike statistics because it is mathematically tractable, is characterized by only two parameters, and generally provides a reasonable fit to RGC (and, to a lesser extent, LGN) IIH's.[15] We have therefore made use of it as a point of departure for incorporating fractal behavior.

B. Prior Evidence for Nonrenewal and Fractal Behavior

Even in the short term, however, it has long been recognized that the renewal assumption is not entirely valid. Kuffler *et al.*[1] showed that the first serial-correlation coefficient was negative for the maintained discharge, a finding confirmed in many subsequent studies. (All serial-correlation coefficients for any renewal process, including the GRP, are, of course, zero.) Troy and Robson[16] presented a sequence of higher-order serial-correlation coefficients (the fourth through the tenth) that are on the positive side (see Figure 6 on page 544 of their paper), thereby providing additional evidence for nonrenewal behavior. Our simulations show that FSPP's can behave precisely in this manner.

In retrospect, there have been several subtle hints of excess low-frequency fluctuations in various measurements. One is the average value of the Fourier components calculated for a collection of LGN spike trains, presented by Troy[18]; the 0.33-Hz component is slightly elevated in comparison with the components at higher frequencies (see Figure 3 on page 406 of his paper). Another is found in Levine and Troy's[21] RSD curves, for which a sample duration of 30 s was used (see Figure 3 on page 346 of their paper). They found that 29 of the 48 dorsal LGN cells that they examined, in their words (page 347), "... provided plots in which the points from the sampled spike train fell along an approximately horizontal line located above the prediction for a renewal process. This is an indicator of substantial low frequency components in the maintained discharge. These components were considered to reflect non-stationarity and were removed ...." An approximately horizontal line for the RSD curve corresponds to $\alpha \sim 1$ $[F(T) \propto T^1]$ (see Subsection 3.C.2). Fractal behavior is indeed apparent in our LGN FF at $T = 30$ s, as is evident in Fig. 6(b). We conclude that fractal behavior was very likely present in the original data sets collected by Levine and Troy but was considered to reflect nonstationarity and was therefore excised.

C. Fractal Shot-Noise-Driven Doubly Stochastic Poisson Model

A nonrenewal, physiologically plausible, alternative to the GRP that is suitable for modeling the short-term behavior of RGC and LGN spike trains is the refractoriness-modified shot-noise-driven doubly stochastic Poisson process (RM-SNDP).[11,14] It incorporates four features known to be operative in the retina[7]—Poisson quantum fluctuations, additive Poisson dark noise, multiplication noise (random multiple neural spikes per absorbed quantum), and refractoriness—and is therefore characterized by four parameters. As mentioned in Subsection 4.A, the agreement of the predictions of this model with short-term measures of the spike train, such as the IIH, is substantially superior to that achievable with the GRP, particularly at low firing rates where C is large and the gamma parameter $r < 1$. Moreover, the RM-SNDP provides a substrate for understanding how the RGC might participate in the psychophysical detection of dim flashes of light.[81] The SNDP imparts gain to the RGC while maintaining the essential proportionality of count variance to mean,[7,14] thereby preserving the deVries–Rose law at low light levels.[81] The rod,[82] and the central neural processing system,[83] apparently behave similarly.

It might therefore be preferable to build a model around the SNDP rather than the GRP. There are two straightforward ways in which this could be carried out. One is to modulate the mean of the SNDP by a process such as FBN or FLN, in much the same way as the FBNDG is generated using a gamma-distributed kernel. The second way is to impart a power-law decaying tail to
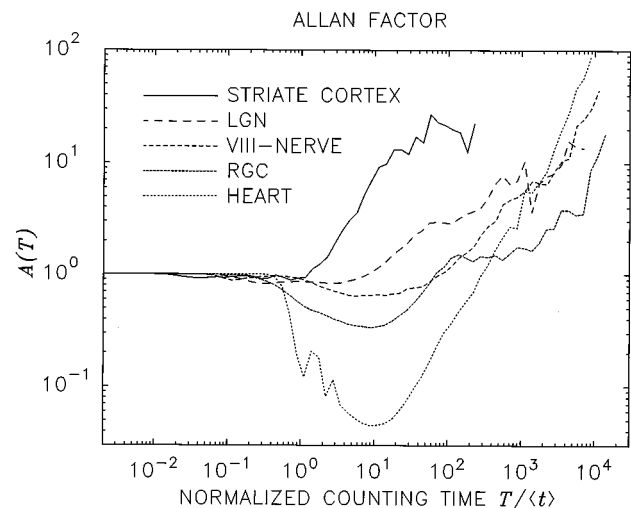

Fig. 12. Comparison of AF's (normalized-time abscissa) for several biological systems exhibiting fractal behavior: cat striate-cortex spike train (solid curve, adapted from Teich *et al.*[25]), cat LGN spike train [long-dashed curve, data from Fig. 7(b)], cat primary auditory-nerve-fiber spike train (VIII-NERVE, medium-dashed curve, adapted from Lowen and Teich[31]), cat RGC spike train [short-dashed curve, data from Fig. 7(a)], and sequence of human heartbeats (HEART, dotted curve, adapted from Turcott and Teich[43]). For longer counting times all of these AF's show the power-law increase characteristic of fractal behavior. The dip in some of these curves, in the vicinity of a normalized counting time of 10, is associated with refractoriness, which serves to regularize the events and reduce the variance in the vicinity of these counting times.

the impulse-response function in the SNDP model. This approach would lead to a variation of the refractoriness-modified fractal shot-noise-driven point process (RM-FSNDP) that we have used earlier in other contexts.[84] The relative merits of these approaches will have to be evaluated.

D. Significance of Fractal Behavior

Fractal behavior is present in all of the RGC and LGN neural spike trains that we have examined, provided that they are of sufficient length. It is interesting to forge a comparison with some other biological systems in which fractal behavior is observed. In Fig. 12 we present AF curves (with normalized-time abscissa) for spike trains from a cat striate-cortex neuron[25] (solid curve), a cat LGN neuron [long-dashed curve, data from Fig. 7(b)], a cat primary auditory-nerve fiber[31] (VIII-NERVE, medium-dashed curve), a cat RGC [short-dashed curve, data from Fig. 7(a)], and for the sequence of human heartbeats[43] (HEART, dotted curve). All of these AF curves increase in fractional power-law fashion for long counting times, revealing similar fractal behavior in all of these preparations. The appearance of fractal behavior at synapses,[39] as well as in systems comprising collections of synapses, indicates that it is an inherent property of neuronal signaling. The use of the AF and its generalization, the WAF,[61] as analysis tools mitigates against nonstationarity as the underlying cause of these fluctuations.

The connection between fractal fluctuations, and information encoding and transmission in neurons, if there is one, remains unclear. Fractal noise exhibits larger fluctuations at lower frequencies and thereby generally renders difficult the detection of the slowest, most gradual changes in a signal. Thus fractal exocytic activity[39] could represent a fundamental source of noise ubiquitous in living cells, to which natural systems must adapt. However, many natural signals are themselves fractal, and it is possible that fractal activity in neurons provides some advantages in terms of matching the detection system to the expected signal.[27,28]

Fractal activity also represents a form of memory because the occurrence of an event at a particular time increases the likelihood of another occurring at some time later, with power-law decaying strength. How such memory might be used at higher centers of the visual system awaits the results of further studies.

REFERENCES

1. S. W. Kuffler, R. FitzHugh, and H. B. Barlow, "Maintained activity in the cat's retina in light and darkness," J. Gen. Physiol. **40**, 683–702 (1957).
2. J. M. Fuster, A. Herz, and O. D. Creutzfeldt, "Interval analysis of cell discharge in spontaneous and optically modulated activity in the visual system," Arch. Ital. Biol. **103**, 159–177 (1965).
3. G. Gestri, L. Maffei, and D. Petracchi, "Spatial and temporal organization in retinal units," Kybernetik (Biol. Cybern.) **3**, 196–202 (1966).
4. R. W. Rodieck, "Maintained activity of cat retinal ganglion cells," J. Neurophysiol. **30**, 1043–1071 (1967).
5. H. B. Barlow and W. R. Levick, "Three factors limiting the reliable detection of light by retinal ganglion cells of the cat," J. Physiol. (London) **200**, 1–24 (1969).
6. H. B. Barlow and W. R. Levick, "Changes in the maintained discharge with adaptation level in the cat retina," J. Physiol. (London) **202**, 699–718 (1969).
7. H. B. Barlow, W. R. Levick, and M. Yoon, "Responses to single quanta of light in retinal ganglion cells of the cat," Vis. Res. **11** (Suppl. 3), 87–101 (1971).
8. W. R. Levick, "Maintained discharge in the visual system and its role for information processing," in *Handbook of Sensory Physiology*, Vol. VII/3, *Central Processing of Visual Information*, Part A, R. Jung, ed. (Springer-Verlag, New York, 1973), pp. 575–598.
9. T. Sato, M. Yamamoto, and H. Nakahama, "Variability of interspike intervals of cat's on-center optic track fibres activated by steady light spot: a comparative study on X- and Y-fibers," Exp. Brain Res. **24**, 285–293 (1976).
10. M. C. Teich, L. Matin, and B. I. Cantor, "Refractoriness in the maintained discharge of the cat's retinal ganglion cell," J. Opt. Soc. Am. **68**, 386–402 (1978).
11. M. C. Teich and B. E. A. Saleh, "Interevent-time statistics for shot-noise-driven self-exciting point processes in photon detection," J. Opt. Soc. Am. **71**, 771–776 (1981).
12. D. N. Mastronarde, "Correlated firing of cat retinal ganglion cells. I. Spontaneously active inputs to X- and Y-cells," J. Neurophysiol. **49**, 303–324 (1983).
13. L. J. Frishman and M. W. Levine, "Statistics of the maintained discharge of cat retinal ganglion cells," J. Physiol. (London) **339**, 475–494 (1983).
14. B. E. A. Saleh and M. C. Teich, "Multiplication and refractoriness in the cat's retinal-ganglion-cell discharge at low light levels," Biol. Cybern. **52**, 101–107 (1985).
15. J. G. Robson and J. B. Troy, "Nature of the maintained discharge of Q, X, and Y retinal ganglion cells of the cat," J. Opt. Soc. Am. A **4**, 2301–2307 (1987).
16. J. B. Troy and J. G. Robson, "Steady discharges of X and Y retinal ganglion cells of cat under photopic illuminance," Visual Neurosci. **9**, 535–553 (1992).
17. P. O. Bishop, W. R. Levick, and W. O. Williams, "Statistical analysis of the dark discharge of lateral geniculate neurones," J. Physiol. (London) **170**, 598–612 (1964).
18. J. B. Troy, "Spatial contrast sensitivities of X and Y type neurones in the cat's dorsal lateral geniculate nucleus," J. Physiol. (London) **344**, 399–417 (1983).
19. R. W. McCarley, O. Benoit, and G. Barrionuevo, "Lateral geniculate nucleus unitary discharge in sleep and waking: state- and rate-specific effects," J. Neurophysiol. **50**, 798–818 (1983).
20. J. Munemori, K.-i. Hara, M. Kimura, and R. Sato, "Statistical features of impulse trains in cat's lateral geniculate neurons," Biol. Cybern. **50**, 167–172 (1984).
21. M. W. Levine and J. B. Troy, "The variability of the maintained discharge of cat dorsal lateral geniculate cells," J. Physiol. (London) **375**, 339–359 (1986).
22. M. C. Teich and S. M. Khanna, "Pulse-number distribution for the neural spike train in the cat's auditory nerve," J. Acoust. Soc. Am. **77**, 1110–1128 (1985).
23. S. B. Lowen and M. C. Teich, "Estimation and simulation of fractal stochastic point processes," Fractals **3**, 183–210 (1995).
24. M. C. Teich, D. H. Johnson, A. R. Kumar, and R. G. Turcott,

"Rate fluctuations and fractional power-law noise recorded from cells in the lower auditory pathway of the cat," Hear. Res. **46**, 41–52 (1990).

25. M. C. Teich, R. G. Turcott, and R. M. Siegel, "Temporal correlation in cat striate-cortex neural spike trains," IEEE Eng. Med. Biol. Mag. **15** (No. 5), 79–87 (1996).

26. R. G. Turcott, P. D. R. Barker, and M. C. Teich, "Long-duration correlation in the sequence of action potentials in an insect visual interneuron," J. Stat. Comput. Simul. **52**, 253–271 (1995).

27. M. C. Teich, "Fractal character of the auditory neural spike train," IEEE Trans. Biomed. Eng. **36**, 150–160 (1989).

28. M. C. Teich, "Fractal neuronal firing patterns," in *Single Neuron Computation*, T. McKenna, J. Davis, and S. Zornetzer, eds. (Academic, Boston, 1992), pp. 589–625.

29. A. R. Kumar and D. H. Johnson, "Analyzing and modeling fractal intensity point processes," J. Acoust. Soc. Am. **93**, 3365–3373 (1993).

30. O. E. Kelly, D. H. Johnson, B. Delgutte, and P. Cariani, "Fractal noise strength in auditory-nerve fiber recordings," J. Acoust. Soc. Am. **99**, 2210–2220 (1996).

31. S. B. Lowen and M. C. Teich, "The periodogram and Allan variance reveal fractal exponents greater than unity in auditory-nerve spike trains," J. Acoust. Soc. Am. **99**, 3585–3591 (1996).

32. N. L. Powers, R. J. Salvi, and S. S. Saunders, "Discharge rate fluctuations in the auditory nerve of the chinchilla," in *Abstracts of the XIVth Midwinter Research Meeting, Association for Research in Otolaryngology* D. J. Lim, ed. (Association for Research in Otolaryngology, Des Moines, Ia., 1991); Abstract No. 411, p. 129.

33. N. L. Powers and R. J. Salvi, "Comparison of discharge rate fluctuations in the auditory nerve of chickens and chinchillas," in *Abstracts of the XVth Midwinter Research Meeting, Association for Research in Otolaryngology* D. J. Lim., ed. (Association for Research in Otolaryngology, Des Moines, Ia., 1992), Abstract No. 292, p. 101.

34. J. B. Bassingthwaighte, L. S. Liebovitch, and B. J. West, *Fractal Physiology* (Oxford U. Press, New York, 1994).

35. B. J. West and W. Deering, "Fractal physiology for physicists: Lévy statistics," Phys. Rep. **246**, 1–100 (1994).

36. L. S. Liebovitch and T. I. Tóth, "Using fractals to understand the opening and closing of ion channels," Ann. Biomed. Eng. **18**, 177–194 (1990).

37. S. B. Lowen and M. C. Teich, "Fractal auditory-nerve firing patterns may derive from fractal switching in sensory hair-cell ion channels," in *Noise in Physical Systems and* 1/*f Fluctuations*, P. H. Handel and A. L. Chung, eds., AIP Conf. Proc. **285** (American Institute of Physics, New York, 1993), pp. 781–784.

38. S. B. Lowen and M. C. Teich, "Fractal renewal processes," IEEE Trans. Inf. Theory **39**, 1669–1671 (1993).

39. S. B. Lowen, S. S. Cash, M.-m. Poo, and M. C. Teich, "Neuronal exocytosis exhibits fractal behavior," in *Computational Neuroscience: Trends in Research 1966*, J. M. Bower, ed. (Plenum, New York) (to be published).

40. M. E. Wise, "Spike interval distributions for neurons and random walks with drift to a fluctuating threshold," in *Statistical Distributions in Scientific Work*, C. E. A. Taillie, ed. (Reidel, Boston, 1981), Vol. 6, pp. 211–231.

41. F. Grüneis, M. Nakao, Y. Mizutani, M. Yamamoto, M. Meesmann, and T. Musha, "Further study on 1/*f* fluctuations observed in central single neurons during REM sleep," Biol. Cybern. **68**, 193–198 (1993).

42. R. G. Turcott and M. C. Teich, "Long-duration correlation and attractor topology of the heartbeat rate differ for normal patients and those with heart failure," in *Chaos in Biology and Medicine*, W. L. Ditto, ed., Proc. SPIE **2036**, 22–39 (1993).

43. R. G. Turcott and M. C. Teich, "Fractal character of the electrocardiogram: distinguishing heart-failure and normal patients," Ann. Biomed. Eng. **24**, 269–293 (1996).

44. E. Kaplan and R. M. Shapley, "X and Y cells in the lateral geniculate nucleus of macaque monkeys," J. Physiol. (London) **330**, 125–143 (1982).

45. E. G. Merrill and A. Ainsworth, "Glass-coated platinum-plated tungsten microelectrodes," Med. Biol. Eng. **10**, 662–672 (1972).

46. S. Hochstein and R. M. Shapley, "Quantitative analysis of retinal ganglion cell classifications," J. Physiol. (London) **262**, 237–264 (1976).

47. R. M. Shapley and S. Hochstein, "Visual spatial summation in two classes of geniculate cells," Nature (London) **256**, 411–413 (1975).

48. D. R. Cox and P. A. W. Lewis, *The Statistical Analysis of Series of Events* (Methuen, London, 1966).

49. F. A. Haight, *Handbook of the Poisson Distribution* (Wiley, New York, 1967).

50. B. E. A. Saleh and M. C. Teich, "Multiplied-Poisson noise in pulse, particle, and photon detection," Proc. IEEE **70**, 229–245 (1982).

51. L. M. Ricciardi and F. Esposito, "On some distribution functions for non-linear switching elements with finite dead time," Kybernetik (Biol. Cybern.) **3**, 148–152 (1966).

52. H. E. Hurst, "Long-term storage capacity of reservoirs," Trans. Am. Soc. Civ. Eng. **116**, 770–808 (1951).

53. W. Feller, "The asymptotic distribution of the range of sums of independent random variables," Ann. Math. Stat. **22**, 427–432 (1951).

54. B. B. Mandelbrot, *The Fractal Geometry of Nature* (Freeman, San Francisco, 1983).

55. H. E. Schepers, J. H. G. M. van Beek, and J. B. Bassingthwaighte, "Four methods to estimate the fractal dimension from self-affine signals," IEEE Eng. Med. Biol. Mag. **11**, 57–71 (1992).

56. J. B. Bassingthwaighte and G. M. Raymond, "Evaluating rescaled range analysis for time series," Ann. Biomed. Eng. **22**, 432–444 (1994).

57. E. Parzen, *Stochastic Processes* (Holden-Day, San Francisco, 1964).

58. P. R. Prucnal and M. C. Teich, "Refractory effects in neural counting processes with exponentially decaying rates," IEEE Trans. Syst. Man Cybern. **SMC-13**, 1028–1033 (1983).

59. U. Fano, "Ionization yield of radiations. II. The fluctuations of the number of ions," Phys. Rev. **72**, 26–29 (1947).

60. E. R. Sanseverino, L. F. Agnati, M. G. Maioli, and C. Galletti, "Maintained activity of single neurons in striate and non-striate areas of the cat visual cortex," Brain Res. **54**, 225–242 (1973).

61. M. C. Teich, C. Heneghan, S. B. Lowen, and R. G. Turcott, "Estimating the fractal exponent of point processes in biological systems using wavelet- and Fourier-transform methods," in *Wavelets in Medicine and Biology*, A. Aldroubi and M. Unser, eds. (CRC Press, Boca Raton, Fla., 1996), Chap. 14, pp. 383–412.

62. D. W. Allan, "Statistics of atomic frequency standards," Proc. IEEE **54**, 221–230 (1966).

63. W. H. Press, B. P. Flannery, S. A. Teukolsky, and W. T. Vetterling, *Numerical Recipes in C* (Cambridge U. Press, New York, 1988).

64. D. E. Nelsen, "Calculation of power spectra for a class of randomly jittered waveforms," in Quarterly Progress Rep. 76 (MIT Research Laboratory of Electronics, Cambridge, Mass., 1964), pp. 168–179.

65. T. Lukes, "The statistical properties of sequences of stochastic pulses," Proc. Phys. Soc. London **78**, 153–168 (1961).

66. F. Frontera and F. Fuligni, "The effect of dead time on the power spectral density estimates of discrete time series," Nucl. Instrum. Methods **157**, 557–561 (1978).

67. M. C. Teich, B. E. A. Saleh, and J. Peřina, "Role of primary excitation statistics in the generation of antibunched and sub-Poisson light," J. Opt. Soc. Am. B **1**, 366–388 (1984).

68. D. R. Cox, *Renewal Theory* (Methuen, London, 1962), p. 8.

69. P. O. Bishop, W. Burke, and R. Davis, "Synapse discharge by single fibre in mammalian visual system," Nature (London) **182**, 728–730 (1958).

70. D. H. Hubel and T. N. Wiesel, "Integrative action in the cat's lateral geniculate body," J. Physiol. (London) **155**, 385–398 (1961).

71. B. G. Cleland, M. W. Dubin, and W. R. Levick, "Sustained

and transient neurones in the cat's retina and lateral geniculate nucleus," J. Physiol. (London) **217**, 473–496 (1971).

72. B. B. Lee, V. Virsu, and O. D. Creutzfeldt, "Linear signal transmission from prepotentials to cells in the macaque lateral geniculate nucleus," Exp. Brain Res. **52**, 50–56 (1983).

73. E. Kaplan and R. Shapley, "The origin of the S (slow) potential in the mammalian lateral geniculate nucleus," Exp. Brain Res. **55**, 111–116 (1984).

74. B. G. Cleland and B. B. Lee, "A comparison of visual responses of cat lateral geniculate nucleus neurones with those of ganglion cells afferent to them," J. Physiol. (London) **369**, 249–268 (1985).

75. E. Kaplan, P. Mukherjee, and R. Shapley, "Information filtering in the lateral geniculate nucleus," in *Contrast Sensitivity*, R. Shapley and D. Man-Kit Lam, eds. (MIT Press, Cambridge, Mass., 1993), Vol. 5, pp. 183–200.

76. E. Kaplan, K. Purpura, and R. M. Shapley, "Contrast affects the transmission of visual information through the mammalian lateral geniculate nucleus," J. Physiol. (London) **391**, 267–288 (1987).

77. M. C. Teich and P. Diament, "Relative refractoriness in visual information processing," Biol. Cybern. **38**, 187–191 (1980).

78. A. M. Derrington and P. Lennie, "The influence of temporal frequency and adaptation level on receptive field organization of retinal ganglion cells in cat," J. Physiol. (London) **333**, 343–366 (1982).

79. M. C. Teich, R. G. Turcott, and S. B. Lowen, "The fractal doubly stochastic Poisson point process as a model for the cochlear neural spike train," in *The Mechanics and Biophysics of Hearing*, P. Dallos, C. D. Geisler, J. W. Matthews, M. A. Ruggero, and C. R. Steele, eds., Vol. 87 of Lecture Notes in Biomathematics (Springer-Verlag, New York, 1990), pp. 354–361.

80. H. B. Barlow, "Scaling and refractoriness in pulse trains," J. Opt. Soc. Am. **59**, 1500 (1969).

81. M. C. Teich, P. R. Prucnal, G. Vannucci, M. E. Breton, and W. J. McGill, "Multiplication noise in the human visual system at threshold: 1. Quantum fluctuations and minimum detectable energy," J. Opt. Soc. Am. **72**, 419–431 (1982).

82. M. C. Teich and T. Li, "The retinal rod as a chemical photomultiplier," J. Visual Commun. Image Represent. **1**, 104–111 (1990).

83. W. J. McGill and M. C. Teich, "Alerting signals and detection in a sensory network," J. Math. Psychol. **39**, 146–163 (1995).

84. S. B. Lowen and M. C. Teich, "Doubly stochastic Poisson point process driven by fractal shot noise," Phys. Rev. A **43**, 4192–4215 (1991).